



Constraint-following vibration control for robot follow-up support system under force-stiffness interdependence

Zhao Liu^a, Fangfang Dong^{a, ID,*}, Xiaomin Zhao^{b,*}, Jiang Han^a, Ye-Hwa Chen^c

^a School of Mechanical Engineering, Hefei University of Technology, Hefei, 230009, Anhui, PR China

^b School of Automotive and Transportation Engineering, Hefei University of Technology, Hefei, 230009, Anhui, PR China

^c The George W. Woodruff School of Mechanical Engineering, Georgia Institute of Technology, Atlanta, 30332, Georgia, USA



ARTICLE INFO

Keywords:

Constraint-following
Stiffness model
Vibration control
Follow-up support
Thin-walled workpieces machining
Industrial robotics

ABSTRACT

The robot follow-up support system provides a cost-effective and flexible support solution for machining thin-walled workpieces. In the past, however, the control design had been a challenge, mainly due to the difficulty in coping with the complex coupling and time-varying dynamic characteristics of the follow-up support system. This study proposes a novel heterogeneous hybrid stiffness model in a “parallel-serial-parallel” structure, along with a constraint-following control method for vibration suppression. First, a second-order vibration model of the follow-up support system was developed, capturing the primary stiffness characteristics of the system while simplifying the modeling through mass bundling. Second, time-varying stiffness analytical expressions are established for the main stiffness components, including the local workpiece region, gas springs at support modules, and the normal stiffness of the robot end-effector, facilitating real-time substitution in the control process. Third, the controllable air pressure term was separated from both sides of the vibration equation, yielding an equivalent underactuated system, and a constraint-following control algorithm was designed. The simulations demonstrate that the proposed control algorithm meets the servo requirements with high precision.

1. Introduction

Thin-walled components [1] [2] are widely used in fields such as aviation and aerospace, yet their relatively low rigidity often leads to deformation and chatter during machining, which further impacts machining accuracy and surface quality. In mainstream support systems [3] [4], the follow-up support system [5] [6] [7] (as shown in Fig. 1) achieves coordinated motion by driving the support head to follow the processing tool. This approach not only adapts to various surface shapes but also maintains sufficient local stiffness while reducing costs. However, the dynamic characteristics of the follower support system are complex and highly coupled, which presents challenges in providing a more controllable supporting effect.

The primary challenge of this study lies in accurately and efficiently constructing a vibration model for the follow-up support system. Xiao et al. proposed an analytical model for gas support stiffness [8] and described the contact effect between the workpiece and the support head based on Hertz contact theory [9]. Bao et al. [10] developed an iterative finite element model for predicting workpiece deformation, which was applied to error prediction in mirror milling of low-stiffness components. Lin et al. [11] employed

* Corresponding author.

E-mail address: fangfangdong@hfut.edu.cn (F. Dong).

Nomenclature

Constants

α, β	Rayleigh damping coefficients	$F_a(t)$	External axial force on the workpiece
η	The product of the workpiece density, the wall thickness, half the length, and half the width of the workpiece	$F_s(p(t))$	Total support force generated by the air pressure
γ	Adiabatic coefficient for an ideal gas	$k_r(t)$	Equivalent stiffness of the robot
ρ	Density of the workpiece	$k_s(p(t))$	Equivalent stiffness of a single support module as a function of air pressure
a	Half the length of the workpiece	$k_w(t)$	Equivalent stiffness of the workpiece's supported region
b	Half the width of the workpiece	$p(t)$	Air pressure in a single support module
D	Bending stiffness of the workpiece	$w(x, y, t)$	Vibrational displacement of the workpiece at a specified time and position
h	Wall thickness of the workpiece	$x_w(t), y_w(t)$	The trajectory of the external axial force on the workpiece
l	Preset distance of the cylinder piston rod extension	$z_r(t)$	Normal displacement of the robot
m_r	Equivalent mass of the robot	$z_w(t)$	Normal displacement of the workpiece's supported region
m_w	Equivalent mass of the workpiece's supported region	$\bar{z}_w(t)$	Desired normal displacement of the workpiece's supported region
n_s	Number of support modules in the support head	$\dot{z}(t)$	The velocity vector of the follow-up support system
s	Cross-sectional area of the rodless chamber in the cylinder	$e(z, \dot{z}, t)$	Constraint-following error
I	Identity matrix	$R(\theta)$	The rotation matrix that transforms coordinates from the robot's base frame to the end-effector frame
κ_1, κ_2	Control parameters of the constraint-following control algorithm	$z(t)$	The displacement vector of the follow-up support system
m_{s1}	Mass of the part of the support head that follows the workpiece's movement	$p_1(z, \dot{z}, t)$	The minimum-norm air pressure that satisfies the vibration control objective under ideal conditions
m_{s2}	Mass of the part of the support head that follows the robot's movement	$p_2(z, \dot{z}, t)$	Air pressure used to compensate the deviation between the actual and desired states of the system
k_θ	Robot joint stiffness matrix	$J(\theta)$	Robot geometrical Jacobian matrix

Variables

t	Time
x, y	Position coordinates of a point on the workpiece
θ	The vector of robot joint angles

Functions

$\hat{w}(x, y, t)$	Approximate solution of the workpiece's vibrational displacement
--------------------	--

$F_a(t)$	External axial force on the workpiece
$F_s(p(t))$	Total support force generated by the air pressure
$k_r(t)$	Equivalent stiffness of the robot
$k_s(p(t))$	Equivalent stiffness of a single support module as a function of air pressure
$k_w(t)$	Equivalent stiffness of the workpiece's supported region
$p(t)$	Air pressure in a single support module
$w(x, y, t)$	Vibrational displacement of the workpiece at a specified time and position
$x_w(t), y_w(t)$	The trajectory of the external axial force on the workpiece
$z_r(t)$	Normal displacement of the robot
$z_w(t)$	Normal displacement of the workpiece's supported region
$\bar{z}_w(t)$	Desired normal displacement of the workpiece's supported region
$\dot{z}(t)$	The velocity vector of the follow-up support system
$e(z, \dot{z}, t)$	Constraint-following error
$R(\theta)$	The rotation matrix that transforms coordinates from the robot's base frame to the end-effector frame
$z(t)$	The displacement vector of the follow-up support system
$p_1(z, \dot{z}, t)$	The minimum-norm air pressure that satisfies the vibration control objective under ideal conditions
$p_2(z, \dot{z}, t)$	Air pressure used to compensate the deviation between the actual and desired states of the system
$J(\theta)$	Robot geometrical Jacobian matrix
$k_p(\theta)$	Translational stiffness matrix of the robot end-effector expressed in the robot's base coordinate system
${}^E k_p(\theta)$	Translational stiffness matrix of the robot end-effector expressed in the end-effector coordinate system

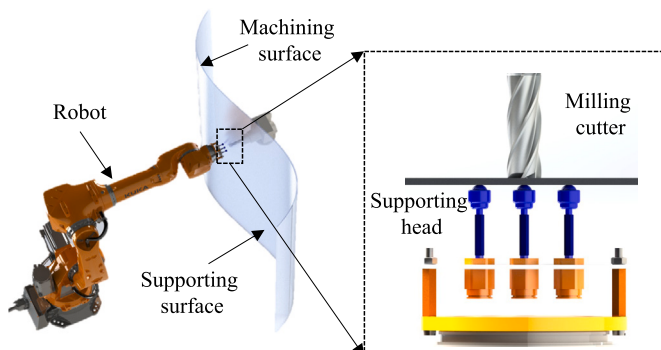


Fig. 1. Follow-up support system.

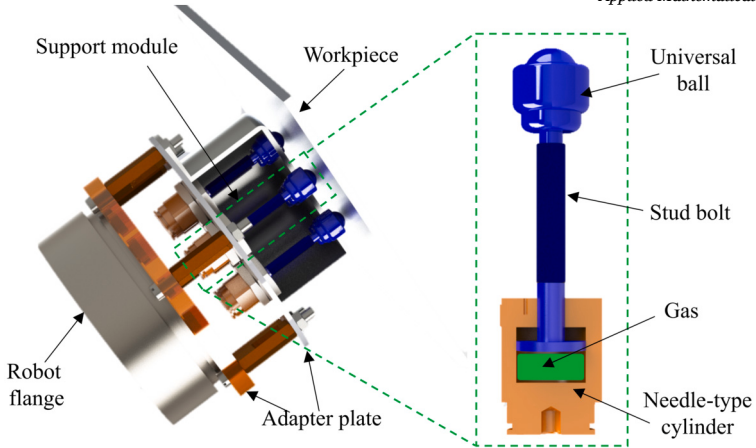


Fig. 2. The structure of the support head.

structural dynamic modification theory to analyze the dynamic response of a workpiece subsystem with additional moving spring dampers. While these studies have effectively characterized the vibration behavior in the vicinity of the machining area, they have yet to account for the stiffness characteristics of the robotic arm [12] [13] that drives the support head. The novelty of this study in terms of modeling lies in the integrated consideration of the coupling relationships among three heterogeneous systems: the workpiece, the support head, and the robot. This paper derives time-varying stiffness analytical expressions for these three systems based on the elastic deformation equation [14], the adiabatic gas state equation [15], and the force-Jacobian mapping of the robot [16]. The vibration model is then constructed through a hybrid series-parallel integration of these components.

Building upon the vibration modeling, the next challenge is to achieve effective vibration suppression. Under offline optimization approaches, extensive research has been conducted on selecting support forces [17], designing the distribution of support points [18], and planning support paths [19]. From another perspective, active control strategies utilizing vibration signal feedback have also demonstrated significant effectiveness. In terms of control strategies, various algorithms such as PID control [20], sliding mode control [21], feedback linearization control [22], and constraint-following control [23] have been widely applied. Among these, constraint-following control is particularly suitable and robust for handling servo constraint problems in nonlinear systems and has been validated in complex dynamic systems, including robots [24], UAVs [25], and vehicles [26]. At the same time, there have been several significant achievements in the optimization of control performance [27] [28] [29]. The main challenge in applying constraint-following control in this study is that adjustments to the controllable part (i.e., air pressure) simultaneously affect both the stiffness matrix and support force of the system. The key innovation of this work lies in separating the air pressure variable within the control equations to obtain an equivalent underactuated system [30] [31] [32] [33], which can then be redesigned for control.

The search for an effective control algorithm has indicated the need for a new framework. This study proposes a novel time-varying dynamic modeling and control design of follow-up support strategies. The main innovations as follows:

- I. A new three-level “serial-parallel-parallel” hybrid vibration model for the follow-up support system is constructed. Building upon the existing contact-area vibration model, we further consider the robot’s dynamic characteristics and simplify the heterogeneous system coupling using mass bundling. Additionally, the analytical expressions for the time-varying stiffness of the workpiece, support head, and robot subsystems are derived.
- II. An active vibration control strategy for the follow-up support system is introduced based on constraint-following theory. By applying variable separation, we transform the force-stiffness dependency issue into an equivalent underactuated system control problem. We obtain the general solution expression for the ideal control term, capture the minimum-norm solution from it, design a feedback control term for the non-ideal state, and prove its asymptotic stability.

2. Modeling of time-varying hybrid stiffness in follow-up support domain

To simplify modeling and capture the primary vibration characteristics, this study focuses on the support region that follows the excitation source. Due to the thin-walled component’s thickness being considerably smaller than its other dimensions, its normal stiffness is significantly lower, leading to more pronounced deformation and vibration. Consequently, this model emphasizes vibrations along the normal direction of the workpiece.

In the follow-up support system, the three main subsystems are the workpiece, support head, and robot. The connection relationships between these subsystems need to be analyzed. The structure of the support head, shown in Fig. 2, consists of multiple support modules arranged in parallel. The entire support head is directly bolted to the robot flange, establishing a serial connection between the support head and the robot. The workpiece, after being clamped at the boundaries, has inherent stiffness in the normal direction. Furthermore, the system composed of the robot and the support head, which contacts the workpiece surface, further enhances the local stiffness in that area, effectively adding a parallel branch to the normal direction of the workpiece. Thus, the follow-up support

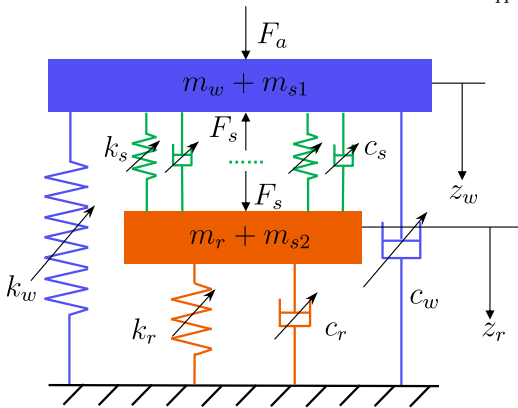


Fig. 3. Three-Level hybrid vibration model of the follow-up support domain.

system is a hybrid system composed in a “parallel-serial-parallel” configuration: multiple support modules are first connected in parallel, then serially connected to the robot, and finally, the entire system is parallel to the supported area of the workpiece.

A single support module is composed of a universal ball and a needle-type cylinder, which are fixed together with bolts. The cylinder is filled with gas, providing support force to the workpiece. Consider the following conditions: during motion, the support head undergoes no axial deformation and does not separate from the workpiece surface. When the workpiece vibrates, it causes the piston rod of the needle-type cylinder to move up and down, creating tension or compression in the gas inside the cylinder. The gas itself thus functions as a “gas spring.” Based on this spring mechanism, we decompose the support head into two parts and apply mass bundling to the workpiece and robot subsystems. The first part of the support head, which moves in contact with the workpiece, includes the piston rod, universal ball, and stud bolt, and its mass is denoted as m_{s1} . The second part, which moves in tandem with the robot’s end-effector, includes the cylinder body, adapter plate, and the outer casing of the support head, with its mass denoted as m_{s2} . This decomposition of the support head better aligns with actual operating conditions and, by bundling the masses, allows us to treat the contact forces between subsystems as internal forces, simplifying the analysis process. In summary, we establish the “mass-spring-damper” vibration model for the follow-up support domain, as shown in Fig. 3.

Remark 1. In previous studies [9] [11], the vibration modeling of the contact area has been proven to be reliable and effective. However, the time-varying dynamic characteristics resulting from the pose changes of the industrial robot while driving the support head cannot be ignored. In this study, we incorporate the robot into the vibration model. Additionally, we establish the hybrid relationship between subsystems based on the structural characteristics of the follow-up support system, which represents an innovation of this research.

We employ the separation method to derive the equations of motion for the two mass subsystems. For the workpiece and the part of supporting head that moves in contact with the workpiece, applying Newton’s second law yields

$$(m_w + m_{s1})\ddot{z}_w(t) = F_a(t) - F_s(p(t)) - k_w(t)z_w(t) - c_w(t)\dot{z}_w(t) - n_s k_s(p(t))(z_w(t) - z_r(t)) - n_s c_s(t)(\dot{z}_w(t) - \dot{z}_r(t)), \quad (1)$$

where t is time, F_a is the external axial force, and F_s is the total support force. m_w , x_w , k_w , and c_w represent the equivalent mass, normal displacement, equivalent stiffness, and equivalent damping of the supported region of the workpiece, respectively. k_s and c_s are the equivalent stiffness and damping of a single support module. z_r is the normal displacement of the robot, and n_s is the number of support modules in the support head. $p(t)$ is the air pressure in a single support module.

Simultaneously, for the robot and the part of supporting head moving in contact with the robot, we have

$$(m_{s2} + m_r)\ddot{z}_r(t) = F_s(p(t)) - k_r(t)z_r(t) - c_r(t)\dot{z}_r(t) - n_s k_s(p(t))(z_r(t) - z_w(t)) - n_s c_s(t)(\dot{z}_r(t) - \dot{z}_w(t)), \quad (2)$$

where m_r , k_r , and c_r represent the equivalent mass, equivalent stiffness, and equivalent damping of the robot, respectively.

By combining Eqs. (1) and (2) and applying the Rayleigh damping model [34], the system’s vibration equation is derived as follows

$$\mathbf{m}\ddot{\mathbf{z}}(t) + \underbrace{(\alpha\mathbf{m} + \beta\mathbf{k}(p(t), t))}_{\text{Rayleigh damping model}} \dot{\mathbf{z}}(t) + \mathbf{k}(p(t), t)\mathbf{z}(t) = \mathbf{F}(p(t), t), \quad (3)$$

with

$$\mathbf{m} = \begin{bmatrix} m_w + m_{s1} & 0 \\ 0 & m_r + m_{s2} \end{bmatrix}, \mathbf{F}(p(t), t) = \begin{bmatrix} F_a(t) - F_s(p(t)) \\ F_s(p(t)) \end{bmatrix},$$

$$\mathbf{z}(t) = \begin{bmatrix} z_w(t) \\ z_r(t) \end{bmatrix}, \mathbf{k}(p(t), t) = \begin{bmatrix} k_w(t) + n_s k_s(p(t)) & -n_s k_s(p(t)) \\ -n_s k_s(p(t)) & n_s k_s(p(t)) + k_r(t) \end{bmatrix},$$

where α and β are the Rayleigh damping coefficients.

Remark 2. For variable stiffness systems, the determination of the Rayleigh damping coefficients can be approached in the following ways: When the stiffness variation is small or the damping accuracy requirement is not high, the two-point frequency method [35] can be used to determine the values of the coefficients at a representative stiffness. When the stiffness switches between several discrete levels, the coefficients for each level can be pre-calculated and accessed through a lookup table during the control process based on the current state. When the stiffness changes continuously and high damping accuracy is required, the dynamic damping ratio and frequency can be computed and updated in real-time for the coefficients [36]. If the real-time computation is too costly or difficult to implement, multi-modal free decay experiments can be conducted offline, and the overall optimal solution can be obtained using the weighted least squares method [37].

Compared to traditional template-based support and multi-point array support, follow-up support is a dynamic system. During the support process, physical variables such as the position of the workpiece's supported domain, the robot end-effector's pose, and the air pressure in the support head are all time-varying. For a more accurate prediction and analysis of the vibration characteristics of follow-up support, Subsections 2.1 to 2.3 will respectively derive the analytical expressions for the stiffness values k_w , k_s , and k_r .

2.1. Equivalent stiffness of local workpiece region

The stiffness of thin-walled components refers to their resistance to deformation at various locations when boundary clamping is applied. In this study, the Galerkin method is employed to derive an approximate analytical solution for the equivalent stiffness of the workpiece along the external force trajectory $(x_w(t), y_w(t))$. Based on the Kirchhoff-Love Assumptions [14], the partial differential equation governing the vibration of the workpiece is formulated as follows

$$D\nabla^4 w(x, y, t) + \rho h \frac{\partial^2 w(x, y, t)}{\partial t^2} = F_0(t)\delta(x - x_w(t))\delta(y - y_w(t)), \quad (4)$$

where D , ρ , and h represent the bending stiffness, density, and wall thickness of the workpiece, respectively. $w(x, y, t)$ denotes the vibrational displacement of the workpiece at position (x, y) and time t . F_0 represents an arbitrary time-varying moving point load, $\delta(\cdot)$ is the Dirac delta function, used to represent the location of point load.

For a rectangular thin plate with length $2a$ and width $2b$, a workpiece coordinate system is defined with the origin at the center of the plate. The boundary conditions for fixed edges can be expressed as

$$\begin{cases} w|_{x=\pm a} = 0, \frac{\partial w}{\partial x}|_{x=\pm a} = 0 \\ w|_{y=\pm b} = 0, \frac{\partial w}{\partial y}|_{y=\pm b} = 0 \end{cases}. \quad (5)$$

Using trigonometric series, a basis function satisfying the boundary conditions (5) is constructed as

$$\phi_{ij}(x, y) = (1 + \cos \frac{i\pi x}{a})(1 + \cos \frac{j\pi y}{b}), \quad i = 1, 3, 5 \dots, \quad j = 1, 3, 5 \dots. \quad (6)$$

The approximate solution \hat{w} of w can then be represented as a linear combination of these basis functions

$$w(x, y, t) \approx \hat{w}(x, y, t) = \sum_i \sum_j C_{ij}(t) \phi_{ij}(x, y), \quad (7)$$

where $C_{ij}(t)$ denotes the coefficients to be determined.

Let $i = j = 1$ in Eq. (7), resulting in only one coefficient C_{11} to solve for, and the expression of \hat{w} is as follows

$$\hat{w} = C_{11}(1 + \cos \frac{\pi x}{a})(1 + \cos \frac{\pi y}{b}). \quad (8)$$

Define the residual R as

$$R = D\nabla^4 \hat{w} + \rho h \frac{\partial^2 \hat{w}}{\partial t^2} - F_0 \delta(x - x_w) \delta(y - y_w). \quad (9)$$

By choosing a weighting function φ identical to the basis function ϕ , the Galerkin method requires setting the inner product of the residual R and φ to zero in order to derive the governing equation:

$$\int_{\Omega} R \varphi d\Omega = 0. \quad (10)$$

Eq. (10) can be expanded to obtain the differential equation with respect to C_{11}

$$9\eta \ddot{C}_{11} + \frac{D\pi^4(3a^4 + 2a^2b^2 + 3b^4)}{a^3b^3} C_{11} = F_0(1 + \cos \frac{\pi x_w}{a})(1 + \cos \frac{\pi y_w}{b}), \quad (11)$$

where η represents the product of the workpiece density ρ , the wall thickness h , half the length a , and half the width b of the workpiece.

By substituting Eq. (8) into Eq. (11) and let $x = x_w$, $y = y_w$, we have

$$\frac{9\eta}{(1 + \cos \frac{\pi x_w}{a})^2 (1 + \cos \frac{\pi y_w}{b})^2} \ddot{w} + \frac{D\pi^4(3a^4 + 2a^2b^2 + 3b^4)}{(1 + \cos \frac{\pi x_w}{a})^2 (1 + \cos \frac{\pi y_w}{b})^2 a^3b^3} \hat{w} = F_0. \quad (12)$$

The coefficient preceding \hat{w} represents the approximate analytical solution for the stiffness

$$k_w(t) \approx \frac{D\pi^4(3a^4 + 2a^2b^2 + 3b^4)}{(1 + \cos \frac{\pi x_w(t)}{a})^2 (1 + \cos \frac{\pi y_w(t)}{b})^2 a^3b^3}. \quad (13)$$

Remark 3. Eq. (7) cleverly transforms the fourth-order partial differential equation (4) into a second-order ordinary differential equation (12) by introducing an approximate solution \hat{w} for the vibration, thereby taking the form of the classic forced vibration equation. In this formulation, the sought stiffness is explicitly expressed (i.e., as the coefficient of displacement). Given that the primary goal of this section is to derive the analytical expressions for the equivalent stiffness at different positions of the workpiece, the displacement \hat{w} serves merely as a bridge, and there is no need to solve it explicitly.

2.2. Equivalent stiffness of support module gas spring

The equivalent stiffness k_s of a single support module primarily originates from the “gas spring” inside the cylinder. This refers to the piston rod of the pin-type cylinder, which, after being extended to a preset distance, retains a volume of gas in the rodless chamber. When the workpiece element vibrates, this gas is stretched or compressed, producing an additional restoring force similar to that of a spring. Based on the classical theory in [15], the expression of k_s can be written as follows:

$$k_s(p(t)) = \frac{\gamma s p(t)}{l}, \quad (14)$$

where γ is the adiabatic coefficient for an ideal gas, s is the cross-sectional area of the rodless chamber in the cylinder, and l is the piston rod extension distance.

2.3. Equivalent stiffness of robot end-effector in the normal direction

During the follow-up support process, the robot’s end-effector remains perpendicular to the workpiece surface. This study focuses on translating the stiffness of each robot joint into its equivalent normal stiffness at the end-effector. Considering an n -degree-of-freedom serial robot with generalized coordinates $\theta(t) = [\theta_1, \theta_2, \dots, \theta_n]^T$, where $\theta_i (i = 1, 2, \dots, n)$ represents the angle of the robot’s i -th joint, the mapping between the external force on the end-effector and the joint torques is first established [16]:

$$\tau(t) = \mathbf{J}^T(\theta(t)) \mathbf{F}_e(t), \quad (15)$$

where $\tau \in \mathbb{R}^n$ is the vector of joint torques, $\mathbf{F}_e \in \mathbb{R}^6$ is the external wrench acting on the robot end-effector, and $\mathbf{J} \in \mathbb{R}^{6 \times n}$ is the geometrical Jacobian matrix of the robot.

Letting χ denote the vector of robot end-effector displacements, taking the total derivative of both sides of Eq. (15) with respect to θ yields

$$\frac{d\tau}{d\theta} = \frac{d\mathbf{J}^T(\theta)}{d\theta} \mathbf{F}_e + \mathbf{J}^T(\theta) \frac{d\mathbf{F}_e}{d\chi} \frac{d\chi}{d\theta}. \quad (16)$$

Incorporating the definitions of stiffness and the geometrical Jacobian, Eq. (16) can be rewritten as

$$\mathbf{k}_\theta = \mathbf{k}_c(\theta) + \mathbf{J}^T(\theta) \mathbf{k}_p(\theta) \mathbf{J}(\theta), \quad (17)$$

where $\mathbf{k}_\theta = \text{diag}(k_{\theta 1}, k_{\theta 2}, \dots, k_{\theta n}) \in \mathbb{R}^{n \times n}$ is the joint stiffness matrix, and $\mathbf{k}_c \in \mathbb{R}^{n \times n}$ represents the complementary stiffness matrix. $\mathbf{k}_p \in \mathbb{R}^{6 \times 6}$ represents the translational stiffness matrix equivalent at the robot end-effector.

For suitable robot postures, \mathbf{k}_c is negligible compared to \mathbf{k}_θ . Given \mathbf{k}_θ and θ , \mathbf{k}_p can be calculated as follows

$$\mathbf{k}_p(\theta) = \mathbf{J}_v^{-T}(\theta) \mathbf{k}_\theta \mathbf{J}_v^{-1}(\theta). \quad (18)$$

Furthermore, the stiffness matrix described in the robot's end-effector coordinate system is obtained as follows

$${}^E \mathbf{k}_p(\theta) = \begin{bmatrix} \mathbf{R}(\theta) & \mathbf{0} \\ \mathbf{0} & \mathbf{R}(\theta) \end{bmatrix}^T \mathbf{k}_p \begin{bmatrix} \mathbf{R}(\theta) & \mathbf{0} \\ \mathbf{0} & \mathbf{R}(\theta) \end{bmatrix}, \quad (19)$$

where $\mathbf{R} \in SO(3)$ represents the rotation matrix that transforms coordinates from the robot's base frame to the end-effector frame.

Assuming that the z -axis of the end-effector frame is aligned with the surface normal, the element ${}^E \mathbf{k}_p(3, 3)$ cannot be directly interpreted as the normal stiffness due to the inherent coupling between translational and rotational components in the robot's stiffness matrix. Instead, an external wrench $\tilde{\mathbf{F}}_e = [0, 0, 1, 0, 0, 0]^T$ should be applied along this direction, and the resulting total linear displacement can be computed using ${}^E \mathbf{k}_p$. The inverse of the displacement norm then yields the effective stiffness along the surface normal direction:

$$k_r(t) = \frac{1}{[{}^E \mathbf{k}_p^{-1} \tilde{\mathbf{F}}_e]_z}, \quad (20)$$

where $[\cdot]_z$ denotes the absolute value of the z -directional component extracted from the six-dimensional displacement vector.

3. Active vibration control based on constraint-following

Through the detailed modeling in Sec. 2, it is evident that the system's vibration is influenced by the trajectory (x_w, y_w) of the external axial force, the robot's joint angles θ , and the air pressure $p(t)$ in a single support module. In the follow-up support machining, the first two factors are pre-planned and designed based on the task requirements. Therefore, the only parameter that can be actively controlled by the designer is $p(t)$. By combining Eqs. (14) and (3), all terms related to $p(t)$ are extracted and organized, resulting in the following equivalent system equation:

$$\mathbf{m}\ddot{\mathbf{z}}(t) + \tilde{\mathbf{c}}(t)\dot{\mathbf{z}}(t) + \tilde{\mathbf{k}}(t)\mathbf{z}(t) + \tilde{\mathbf{F}}(t) = \mathbf{f}(\mathbf{z}(t), \dot{\mathbf{z}}(t))p(t), \quad (21)$$

where

$$\begin{aligned} \tilde{\mathbf{c}}(t) &= \begin{bmatrix} \alpha(m_w + m_{s1}) + \beta k_w(t) & 0 \\ 0 & \alpha(m_r + m_{s2}) + \beta k_r(t) \end{bmatrix}, \\ \tilde{\mathbf{k}}(t) &= \begin{bmatrix} k_w(t) & 0 \\ 0 & k_r(t) \end{bmatrix}, \quad \tilde{\mathbf{F}}(t) = \begin{bmatrix} -F_a(t) \\ 0 \end{bmatrix}, \\ \mathbf{f}(\mathbf{z}(t), \dot{\mathbf{z}}(t)) &= \frac{\beta n_s \gamma s}{l} \begin{bmatrix} -1 & 1 \\ 1 & -1 \end{bmatrix} \dot{\mathbf{z}}(t) + \frac{n_s \gamma s}{l} \begin{bmatrix} -1 & 1 \\ 1 & -1 \end{bmatrix} \mathbf{z}(t) + \begin{bmatrix} -n_s s \\ n_s s \end{bmatrix}. \end{aligned}$$

Remark 4. Reference [8] explores the relationship between air pressure and gas stiffness, while Reference [17] controls the workpiece deformation by adjusting the support force. In these related studies, force and stiffness are considered independently. However, as shown in Eq. (3), the adjustment of $p(t)$ simultaneously affects the support force \mathbf{F} and the stiffness matrix \mathbf{k} , which constitutes a force-stiffness interdependence issue. This makes it challenging to design $p(t)$ via state feedback to control the vibration \mathbf{z} . The equivalent system shown in Eq. (21) separates and extracts the control term, allowing $p(t)$ to appear explicitly and independently on the right-hand side of the equation. It should be noted that, at this point, there is only one control input, while the system model has two state variables to be controlled, z_w and z_r . This transforms the force-stiffness interdependence problem into a control problem for an underactuated system, where \mathbf{f} serves as the system's input matrix.

Considering that the primary task of the follow-up support system is to suppress the vibration of the workpiece, the control task is to design a specific expression for $p(t)$ based on the system's state feedback, so that z_w meets the desired requirements. We formulate the control requirement in the following form as a servo constraint:

$$\dot{z}_w(t) - \bar{z}_w(t) + \kappa_1(z_w(t) - \bar{z}_w(t)) = 0, \quad (22)$$

where $\kappa_1 > 0$, and \bar{z}_w is a target actively designed by the controller to either reduce vibration energy by controlling the amplitude or adjust the vibration frequency to avoid resonance in specific cases.

Eq. (22) can be arranged in matrix form as

$$\mathbf{A}\dot{\mathbf{z}}(t) = \mathbf{d}(\mathbf{z}(t), t), \quad (23)$$

where

$$\mathbf{A} = \begin{bmatrix} 1 & 0 \\ 0 & 0 \end{bmatrix}, \quad \mathbf{d} = \begin{bmatrix} \dot{z}_w - \kappa_1(z_w - \bar{z}_w) \\ 0 \end{bmatrix}.$$

Taking the time derivative of both sides of Eq. (23) results in a second-order constraint

$$\mathbf{A}\ddot{\mathbf{z}}(t) = \mathbf{b}(\dot{\mathbf{z}}(t), t), \quad (24)$$

where

$$\mathbf{b} = \begin{bmatrix} \ddot{\mathbf{z}}_w - \kappa_1(\dot{\mathbf{z}}_w - \dot{\tilde{\mathbf{z}}}_w) \\ 0 \end{bmatrix}.$$

We first explore the control design under ideal conditions.

Definition 1. [38] For given matrix $\mathcal{K} \in \mathbb{R}^{n_1 \times n_2}$ and vector $\mathcal{Y} \in \mathbb{R}^{n_1}$, the equation $\mathcal{K}\mathcal{X} = \mathcal{Y}$ is said to be consistent with respect to \mathcal{X} if there exists at least one solution \mathcal{X} that satisfies the equation.

Assumption 1. For given \mathbf{A} and \mathbf{b} , the constraint (24) is consistent with respect to \mathbf{z} .

This Assumption ensures that, for the given constrained task, the system possesses at least one corresponding solution. That is, the constraints must satisfy the system's physical limitations, be non-conflicting, and be achievable. According to the Lemma A2, it requires $\mathbf{A}\mathbf{A}^\dagger \mathbf{b} = \mathbf{b}$, where the superscript † denotes the Moore-Penrose (MP) inverse of the matrix.

Let $\ddot{\mathbf{v}} = \mathbf{m}^{1/2}\ddot{\mathbf{z}}$ and $\mathbf{a}(\mathbf{z}, \dot{\mathbf{z}}, t) = \mathbf{m}^{-1/2}(-\tilde{\mathbf{c}}\dot{\mathbf{z}} - \tilde{\mathbf{k}}\mathbf{z} - \tilde{\mathbf{F}})$, then system (21) can be rewritten as

$$\ddot{\mathbf{v}} = \mathbf{a} + \mathbf{m}^{-1/2}f p(t). \quad (25)$$

Similarly, let $\Gamma_1 = \mathbf{A}\mathbf{m}^{-1/2}$, then constraint (24) can be rewritten as

$$\Gamma_1 \ddot{\mathbf{v}} = \mathbf{b}. \quad (26)$$

Let $\hat{\mathbf{b}}(\mathbf{z}, \dot{\mathbf{z}}, t) = \mathbf{b}(\mathbf{z}, \dot{\mathbf{z}}, t) - \Gamma_1 \mathbf{a}(\mathbf{z}, \dot{\mathbf{z}}, t)$ and $\Gamma_2(\mathbf{z}, \dot{\mathbf{z}}) = \mathbf{m}^{-1/2}f(\mathbf{z}, \dot{\mathbf{z}})$, then we have

$$(\Gamma_1 \Gamma_2)p(t) = \hat{\mathbf{b}}. \quad (27)$$

Definition 2. [31] For any $(\mathbf{z}, \dot{\mathbf{z}}, t) \in \mathbb{R}^2 \times \mathbb{R}^2 \times \mathbb{R}$, if there exists a control $p(t)$ such that the motion of the system described by equation (25) satisfies the servo constraint (26), then system (25) is *servo constraint controllable*.

Assumption 2. For given Γ_1 , Γ_2 and $\hat{\mathbf{b}}$, Eq. (27) is consistent with respect to $p(t)$.

This Assumption ensures that, for the given system and constraint, there theoretically exists at least one controller capable of achieving the desired requirements. This serves as the necessary condition for our controller design; without it, the control problem becomes unrealistic and unachievable. Similarly, we have $(\Gamma_1 \Gamma_2)(\Gamma_1 \Gamma_2)^\dagger \hat{\mathbf{b}} = \hat{\mathbf{b}}$.

Theorem 1. Based on Assumptions 1 and 2, for any $(\mathbf{z}, \dot{\mathbf{z}}) \in \mathbb{R}^2 \times \mathbb{R}^2$, the system (25) is servo constraint controllable with respect to constraint (26) if and only if $\text{rank}(\Gamma_1 \Gamma_2(\mathbf{z}, \dot{\mathbf{z}})) \geq 1$ is satisfied. The general solution expression for the control is given by

$$p_{gen} = (\Gamma_1 \Gamma_2)^\dagger \hat{\mathbf{b}} + [\mathbf{I} - (\Gamma_1 \Gamma_2)^\dagger (\Gamma_1 \Gamma_2)]\mathbf{S}, \quad (28)$$

where \mathbf{I} is the identity matrix, and $\mathbf{S} \in \mathbb{R}^2$ is an arbitrary vector that may depend on $(\mathbf{z}, \dot{\mathbf{z}}, t)$.

The proof of Theorem 1 is shown in Appendix.

When $\mathbf{I} - (\Gamma_1 \Gamma_2)^\dagger (\Gamma_1 \Gamma_2) \neq \mathbf{0}$, taking the inner product of the two components that constitute p_{gen} , and using the properties of Lemma A1 in the Appendix, we obtain the following result:

$$\langle (\Gamma_1 \Gamma_2)^\dagger \hat{\mathbf{b}}, [\mathbf{I} - (\Gamma_1 \Gamma_2)^\dagger (\Gamma_1 \Gamma_2)]\mathbf{S} \rangle = \mathbf{0}. \quad (29)$$

Thus, we obtain $(\Gamma_1 \Gamma_2)^\dagger \hat{\mathbf{b}} \perp [\mathbf{I} - (\Gamma_1 \Gamma_2)^\dagger (\Gamma_1 \Gamma_2)]\mathbf{S}$, which further leads to

$$\begin{aligned} \|(\Gamma_1 \Gamma_2)^\dagger \hat{\mathbf{b}}\|^2 &\leq \|(\Gamma_1 \Gamma_2)^\dagger \hat{\mathbf{b}}\|^2 + \|[\mathbf{I} - (\Gamma_1 \Gamma_2)^\dagger (\Gamma_1 \Gamma_2)]\mathbf{S}\|^2 \\ &= \|(\Gamma_1 \Gamma_2)^\dagger \hat{\mathbf{b}} + [\mathbf{I} - (\Gamma_1 \Gamma_2)^\dagger (\Gamma_1 \Gamma_2)]\mathbf{S}\|^2 = \|p_{gen}\|. \end{aligned} \quad (30)$$

Therefore, among all feasible ideal control p_{gen} , the one with the minimal norm (i.e., $\mathbf{S} = \mathbf{0}$) is

$$\begin{aligned} p_1(\mathbf{z}, \dot{\mathbf{z}}, t) &= (\Gamma_1 \Gamma_2(\mathbf{z}, \dot{\mathbf{z}}))^\dagger \hat{\mathbf{b}}(\mathbf{z}, \dot{\mathbf{z}}, t) \\ &= (\mathbf{A}\mathbf{m}^{-1}f(\mathbf{z}, \dot{\mathbf{z}}))^\dagger [\mathbf{b}(\mathbf{z}, \dot{\mathbf{z}}, t) + \mathbf{A}\mathbf{m}^{-1}(\tilde{\mathbf{c}}\dot{\mathbf{z}} + \tilde{\mathbf{k}}\mathbf{z} + \tilde{\mathbf{F}})]. \end{aligned} \quad (31)$$

Assumption 3. For a given constant matrix $\mathbf{P} \in \mathbb{R}^{2 \times 2}$ and $\mathbf{P} > 0$, let

$$\Phi(\mathbf{z}, \dot{\mathbf{z}}) = \mathbf{P}\mathbf{A}\mathbf{m}^{-1}f(\mathbf{z}, \dot{\mathbf{z}})f^T(\mathbf{z}, \dot{\mathbf{z}})\mathbf{m}^{-1}\mathbf{A}^T\mathbf{P}, \quad (32)$$

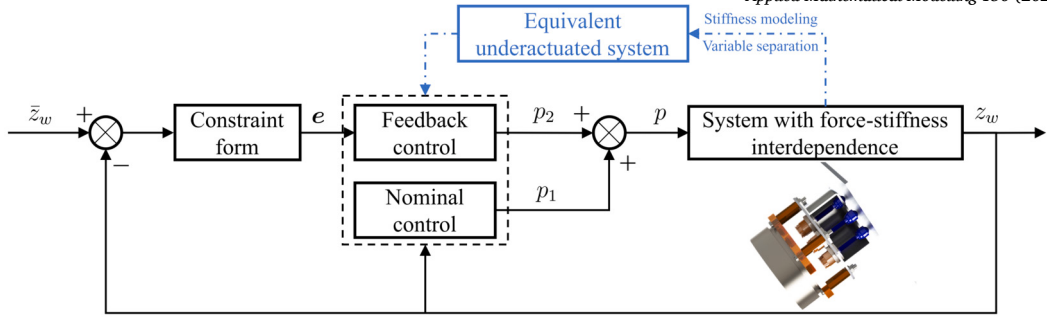


Fig. 4. Follow-up support system vibration control block diagram.

there exists a constant $\underline{\lambda} > 0$, such that for all $(z, \dot{z}) \in \mathbb{R}^2 \times \mathbb{R}^2$,

$$\lambda_m(\Phi(z, \dot{z})) \geq \underline{\lambda}. \quad (33)$$

This Assumption ensures that the minimum eigenvalue of Φ remains at a finite distance from zero, preventing it from approaching zero asymptotically [39]. This guarantees the stability of the control application and prevents issues such as system singularities and degeneration.

Defining the constraint-following error as

$$e(z, \dot{z}, t) = A\dot{z} - d(z, t). \quad (34)$$

We propose the following constraint-following control (CFC) algorithm

$$p(t) = p_1(z, \dot{z}, t) + p_2(z, \dot{z}, t), \quad (35)$$

with

$$p_2(z, \dot{z}, t) = -\kappa_2 f^T(z, \dot{z}) \mathbf{m}^{-1} \mathbf{A}^T \mathbf{P} e(z, \dot{z}, t), \quad (36)$$

where $\kappa_2 > 0$ is a control parameter. p_1 , as given in equation (31), represents the nominal control term with the minimal norm among all candidates. p_2 is the feedback control term, designed to compensate for deviations between the actual and desired system states, specifically for underactuated systems. The control block diagram of the system is illustrated in Fig. 4.

Theorem 2. Let $\tilde{e}(t) = e(z(t), \dot{z}(t), t)$, if the given Assumptions 1-3 are satisfied, then applying the control (35) to system (21), the system satisfies asymptotic stability: For any $\varepsilon > 0$, there exists a $\delta > 0$ such that if $\|\tilde{e}(t_0)\| < \delta$, then for all $t \geq t_0$, $\|\tilde{e}(t)\| < \varepsilon$. Additionally, there exists $\delta' > 0$ such that if $\|\tilde{e}(t_0)\| < \delta'$, then the error satisfies $\lim_{t \rightarrow \infty} \|\tilde{e}(t)\| = 0$.

The proof of Theorem 2 is shown in Appendix.

4. Numerical simulation

This Section is divided into two parts. Sec. 4.1 verifies the accuracy of the three stiffness analytical expressions derived in Sec. 2 and conducts a system stiffness analysis, while Sec. 4.2 verifies the vibration suppression effectiveness of the CFC algorithm proposed in Sec. 3.

4.1. Stiffness model verification and analysis

First, we verify the analytical expression Eq. (13) for the workpiece stiffness k_w (derived from Eqs. (4) to (12)). We select a widely used aluminum alloy plate component, for which the bending stiffness $D = 800 \text{ N} \cdot \text{m}$ is known. The dimensions are set as length $2a = 1\text{m}$, width $2b = 1\text{m}$, and wall thickness $h = 5\text{mm}$, with a width-to-thickness ratio that meets typical thin-walled component characteristics. The workpiece is fixed at all four edges, and a 100 N point load is applied at the center of the workpiece, i.e., $x_w = y_w = 0$. As shown in Fig. 5, the COMSOL finite element simulation results yield a center displacement of $7.02 \times 10^{-4}\text{m}$, while our calculated stiffness is $1.56 \times 10^5 \text{ N/m}$, and the adjusted displacement is $6.41 \times 10^{-4}\text{m}$, with an analytical accuracy of approximately 91.3%.

Building on this, Fig. 6 presents the stiffness distribution within the plane of the entire workpiece. The stiffness decreases significantly from the boundary to the center, exhibiting a pronounced ring-like decay trend, with the weakest stiffness magnitude ranging between 10^5 and 10^6 N/m .

Next, we verify the analytical expression Eq. (14) for the stiffness of a single support module k_s . We set the piston rod extension distance $l = 0.01\text{m}$, the cross-sectional area of the rodless chamber $s = \pi \cdot 10^{-4}\text{m}^2$, the gas pressure inside the chamber is 10^5 pa , and

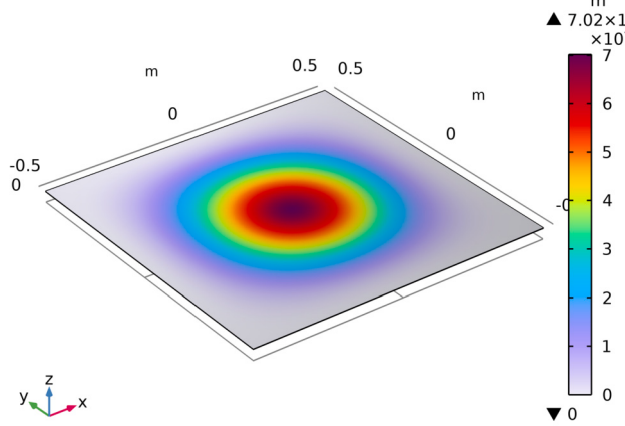


Fig. 5. Workpiece stiffness analytical expression verification.

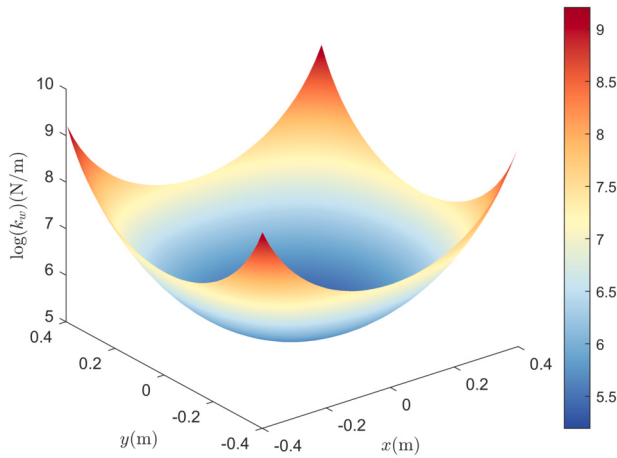


Fig. 6. Distribution of stiffness at various positions on the workpiece.

the adiabatic coefficient of the ideal gas $\gamma = 1.4$. A 5 N pressure is applied along the piston rod axis. As shown in Fig. 7, the COMSOL finite element simulation results yield a piston rod displacement of 1.14×10^{-3} m, while our calculated stiffness is 4.42×10^3 N/m, and the adjusted displacement is 1.12×10^{-3} m, with an analytical accuracy of approximately 98.2% (this analytical model achieves higher accuracy only when the piston rod undergoes small disturbances).

Building on this, Fig. 8 shows that the equivalent gas stiffness is inversely proportional to the piston rod extension distance and directly proportional to the internal gas pressure, with stiffness values generally in the range of 10^5 N/m. After paralleling multiple support points, the total stiffness provided can reach the order of 10^6 N/m, which is consistent with the stiffness level of the weakest part of the workpiece.

Finally, we verify the analytical expression Eq. (20) for the robot's normal stiffness k_r (derived from Eqs. (15) to (19)). The industrially common KUKA KR70 robot is selected for the simulation, with its kinematic parameters referenced from [5]. The initial state is set as $q = [0, 0, 0, 0, 0, 0]^T$, the joint stiffness is $\text{diag}(200, 90, 100, 6, 2.5, 2) \cdot 10^4$ N·m/rad, and an external force of 100N is applied to the robot's end-effector normal. Since the robot's stiffness exhibits translation-rotation coupling, even when force is applied only to the end-effector normal, the robot's final deformation occurs in space. As shown in Fig. 9, the COMSOL finite element simulation results show a total end-effector displacement of 1.67×10^{-4} m, while the calculated displacement vector in the world coordinate system is $[-9.84 \times 10^{-5}, 4.14 \times 10^{-21}, 1.34 \times 10^{-4}]$ m, with an adjusted total deformation of 1.66×10^{-4} m, giving an analytical accuracy of approximately 99.4%.

Building on this, Fig. 10 displays the distribution of the robot's normal stiffness within its workspace. The stiffness values are evenly distributed between 10^6 N/m and 10^7 N/m, with larger values near the boundaries of the workspace. However, the robot's flexibility significantly decreases as it approaches the boundary. Therefore, when performing actual machining, both the stiffness and flexibility of the robot should be considered together to determine the relative position between the robot and the workpiece.

In summary, the three primary coupled stiffnesses in follow-up support are complex and time-varying, and their magnitudes are comparable. To maintain stable and effective support, control design must account for dynamic parameter variations during machining.

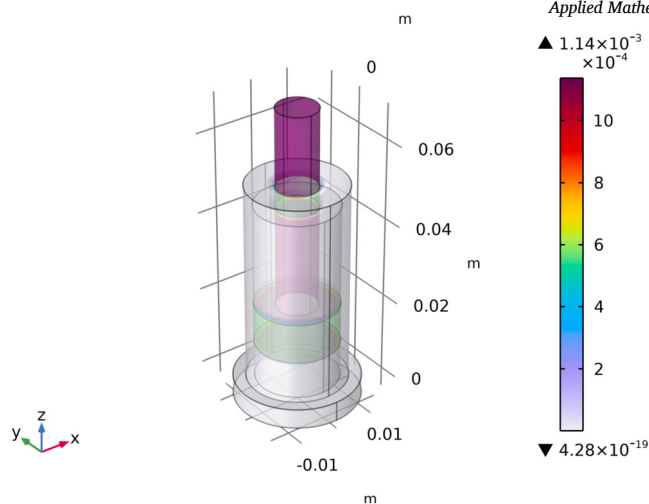


Fig. 7. Support module stiffness analytical expression verification.

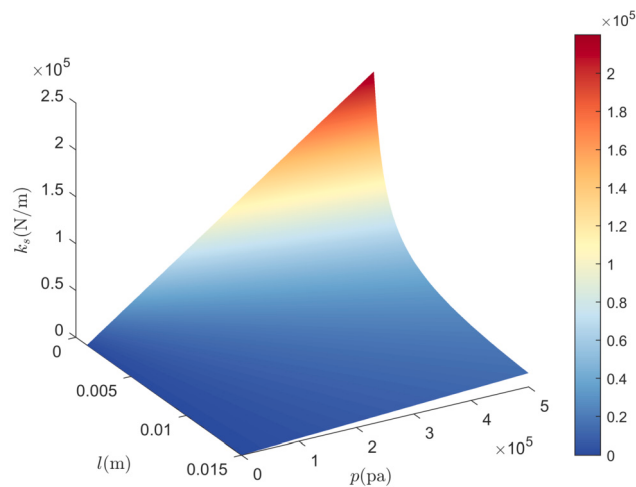


Fig. 8. Relationship between support module stiffness, cylinder extension distance, and input pressure.

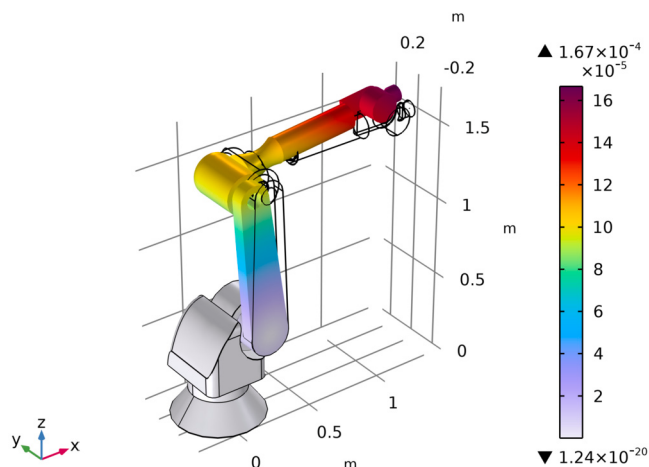


Fig. 9. Verification of the analytical expression for the end-effector stiffness of the robot.

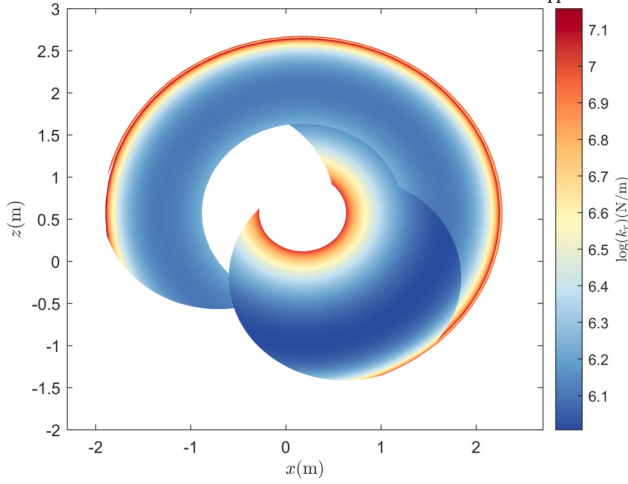


Fig. 10. The distribution of the normal stiffness of the robot end-effector within its workspace.

4.2. Constraint-following control performance analysis

The system vibration model was established through Eqs. (1) to (3), and an equivalent transformed model was derived in Eq. (21). This section primarily aims to verify the effectiveness of the proposed CFC method in Eq. (35), which is derived from Eqs. (22) to (34) and Eq. (36), in suppressing vibration.

Setting $\alpha = \beta = 1$, with mass parameters $m_w = 13.5\text{kg}$, $m_r = 2000\text{kg}$, and $m_{s1} = m_{s2} = 5\text{kg}$, and the number of support modules $n_s = 7$. An external excitation force $F_a = 100 \sin(2\pi t)\text{N}$ is applied, with a moving path in the workpiece coordinate system of $x_w = 0.05t - 0.4\text{m}$ and $y_w = 0\text{m}$, simulating a machining scenario where both the force magnitude and position vary over time.

To clearly demonstrate the advantages of the proposed CFC algorithm, feedback linearization control (FLC) algorithm is selected as comparison strategy. The FLC expressions are as follows

$$p_{FLC}(z, \dot{z}, t) = f(z, \dot{z})^\dagger [mZ(z, \dot{z}, t) + \tilde{c}\dot{z} + \tilde{k}z + \tilde{F}], \quad (37)$$

with

$$Z = \begin{bmatrix} \ddot{\bar{z}}_w \\ 0 \end{bmatrix} + k_d \begin{bmatrix} \dot{\bar{z}}_w - \dot{z}_w \\ 0 \end{bmatrix} + k_p \begin{bmatrix} \bar{z}_w - z_w \\ 0 \end{bmatrix},$$

where $k_d > 0$ is the differential gain coefficient, and $k_p > 0$ is the proportional gain coefficient.

Remark 5. FLC [22] is a widely used classical and effective control strategy. By substituting Eq. (37) into the system Eq. (21), and setting $\hat{e} = \bar{z}_w - z_w$, we obtain $\ddot{\hat{e}} + k_d\dot{\hat{e}} + k_p\hat{e} = 0$, which effectively linearizes the error dynamics of the nonlinear and strongly coupled system. Based on this formulation, by selecting $V = \frac{1}{2}\hat{e}^T k_p \hat{e} + \frac{1}{2}\dot{\hat{e}}^T \dot{\hat{e}} > 0$, it follows that $\dot{V} = -\dot{\hat{e}}^T k_d \dot{\hat{e}} \leq 0$, thereby satisfying the Lyapunov stability.

The parameters of the CFC algorithm are set as $\kappa_1 = 100$, $\kappa_2 = 10^6$ and $P = 100I$, whereas the parameters of the FLC algorithm are set as $k_d = 13888.89$ and $k_p = 55555.56$. To ensure the fairness of the comparison, we optimized the control parameters of the FLC algorithm with the objective of minimizing the root mean square of the tracking error, under the condition that the algorithm achieves stable convergence. The optimization process is illustrated in Fig. 11.

The target trajectory is set to $\bar{z}_w = \sin(t) \cdot 10^{-3}\text{m}$ for $t \in [0, 3\pi]$ s for analysis. The pressure threshold is set to ± 1 MPa. Fig. 12a shows the vibration displacement error of the workpiece. The error curve of the CFC algorithm converges at around 0.5 s, achieving a control accuracy on the order of 10^{-8} . In contrast, the FLC algorithm exhibits noticeable oscillations in the early stage of the error curve, converging at about 2 s, with an accuracy on the order of 10^{-6} . Defining the total position error as $e_{\text{sum}} = \int |z_w(t) - \bar{z}_w(t)| dt$, Fig. 12b indicates that e_{sum} under the CFC algorithm is reduced by approximately 13.15% compared to that under the FLC algorithm.

The control pressure $p(t)$ is shown in Fig. 13a, where both algorithms exhibit significant fluctuations at the onset of control, followed by a converging trend and gradual stabilization. Defining the total control cost as $p_{\text{cost}} = \int |p(t)| dt$, Fig. 13b illustrates that the control cost under the FLC algorithm is reduced by about 4.33% relative to that under the CFC algorithm.

Furthermore, the total error and total cost under different control parameters are shown in Figs. 14 and 15. The influence of the control parameter κ_1 on the total error is relatively small, while the total error initially decreases and then increases as κ_2 increases. On the other hand, reducing both control parameters leads to a decrease in control costs to some extent. In different control scenarios, a comprehensive analysis of the trade-off between accuracy and cost can be performed, with the appropriate control parameters determined through game theory.

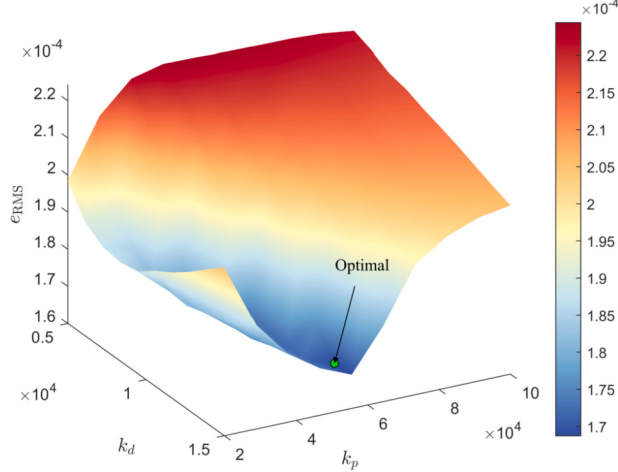
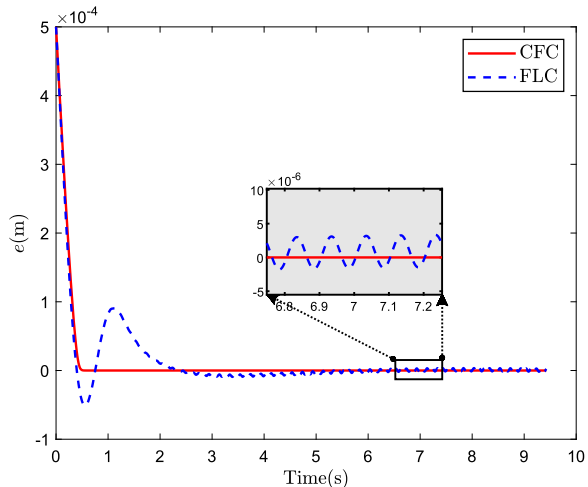
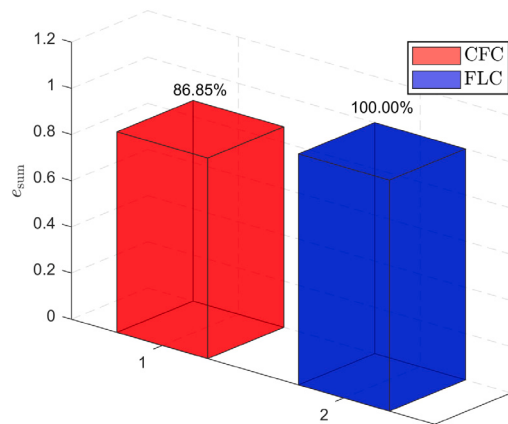


Fig. 11. The control parameters optimization of the FLC algorithm.

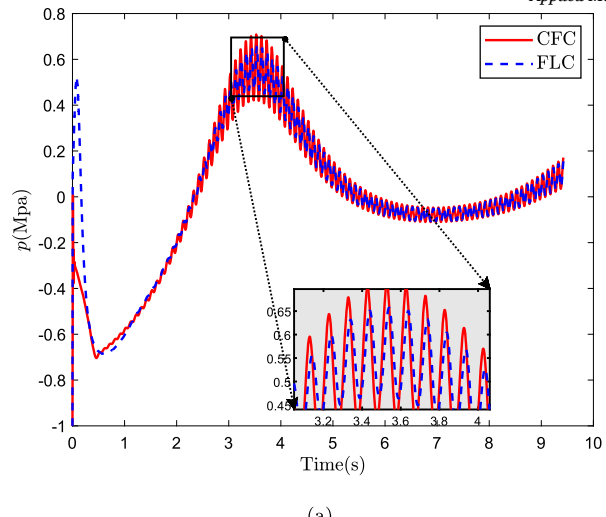


(a)

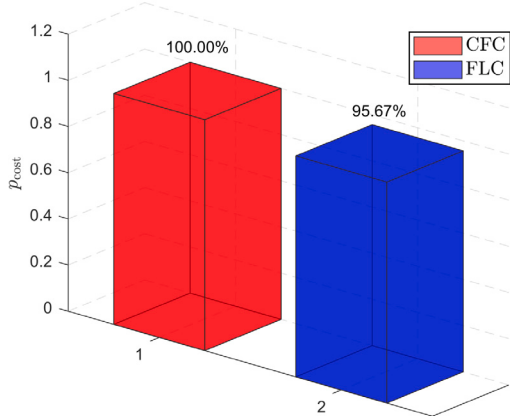


(b)

Fig. 12. Control error.(a) Error curve of vibration displacement. (b) Total error comparison of vibration displacement.



(a)



(b)

Fig. 13. Control cost.(a) Control pressure. (b) Total cost comparison of control pressure.

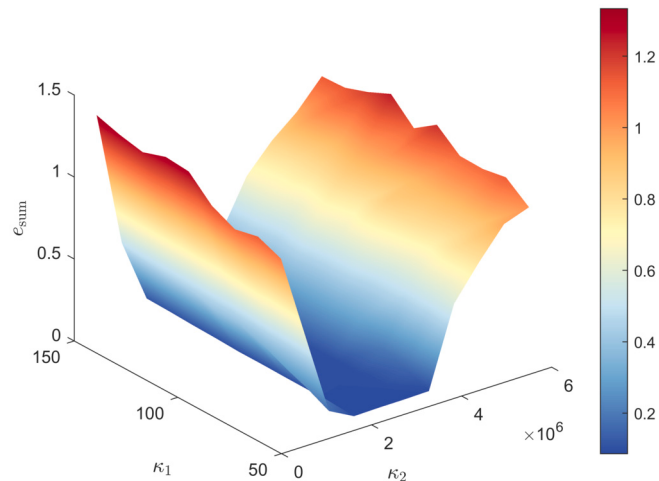


Fig. 14. Total error under different control parameters.

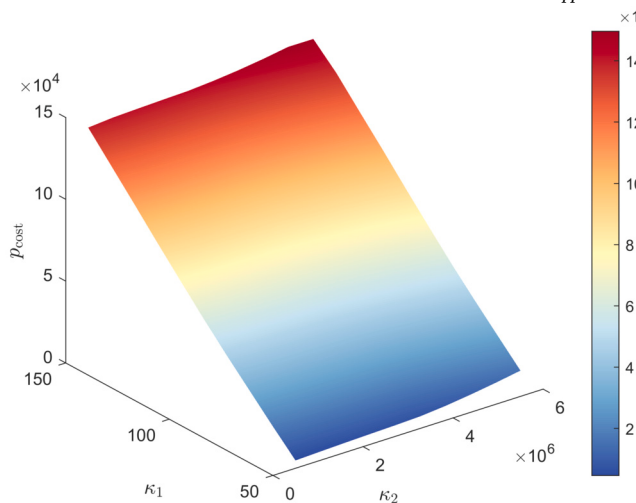


Fig. 15. Total cost under different control parameters.

5. Conclusion

This study proposes a hybrid vibration model and a CFC method to support high-performance compliant support machining of thin-walled components. First, building upon existing contact-region modeling, the dynamic characteristics of the robot are incorporated. Through system analysis and mass lumping, the model is simplified into a second-order hybrid vibration system. Time-varying analytical expressions for three key stiffness components—the local stiffness of the workpiece, the pneumatic spring stiffness at the support modules, and the robot end-effector's normal stiffness—are derived. These explicit formulations are more suitable for real-time control than implicit differential forms. COMSOL simulations verify their accuracy exceeds 90%, and spatial analysis shows stiffness magnitudes mainly lie within $10^6 \text{ N/m} - 10^7 \text{ N/m}$.

Beyond existing works that treat pressure stiffness or support force separately, we reveal their interdependence and reformulate the problem as an equivalent underactuated control task. A CFC algorithm is then developed and proven asymptotically stable. Simulations show state convergence within 0.5 s, a 13.15% reduction in total control error compared to a FLC algorithm, at the cost of a 4.33% increase in control effort.

The main contributions lie in the hybrid modeling and the transformation of the force-stiffness dependency. However, the current model does not yet address pressure control delay or system uncertainties, which will be pursued in future work. Experimental validation and parameter identification on a physical platform will also be conducted to further verify the proposed approach.

CRediT authorship contribution statement

Zhao Liu: Writing – original draft, Software, Methodology, Conceptualization. **Fangfang Dong:** Writing – review & editing, Project administration, Funding acquisition. **Xiaomin Zhao:** Visualization, Funding acquisition. **Jiang Han:** Supervision, Resources. **Ye-Hwa Chen:** Writing – review & editing, Visualization, Formal analysis.

Declaration of competing interest

The authors declare that they have no known competing financial interests or personal relationships that could have appeared to influence the work reported in this paper.

Acknowledgements

This work was supported in part by the National Natural Science Foundation of China under Grant 52275484/52472404, in part by the Anhui Province Science and Technology Breakthrough Plan Project under Grant 202423e09050004, in part by the Natural Science Foundation of Anhui under Grant JZ2024AKZR0540, and in part by the Fundamental Research Funds for the Central Universities under Grant JZ2024HGTG0298/PA2024GDSK0043.

Appendix A

Lemma A1. [40] The matrix $\mathbf{X}_0 \in \mathbb{R}^{n_4 \times n_3}$ is the M-P generalized inverse of matrix $\mathbf{X} \in \mathbb{R}^{n_3 \times n_4}$ if and only if the following hold

$$\mathbf{X} \mathbf{X}_0 \mathbf{X} = \mathbf{X}, \quad (\text{A.1})$$

$$\mathbf{X}_0 \mathbf{X} \mathbf{X}_0 = \mathbf{X}_0,$$
(A.2)

$$(\mathbf{X} \mathbf{X}_0)^T = \mathbf{X}_0 \mathbf{X}, (\mathbf{X}_0 \mathbf{X})^T = \mathbf{X} \mathbf{X}_0.$$
(A.3)

Lemma A2. [38] The equation $\mathcal{K}\mathcal{X} = \mathcal{Y}$ is consistent with respect to \mathcal{X} if and only if $\mathcal{K}\mathcal{K}^\dagger \mathcal{Y} = \mathcal{Y}$.

Proof of Theorem 1. (Sufficiency): Suppose $\text{rank}(\boldsymbol{\Gamma}_1 \boldsymbol{\Gamma}_2) \geq 1$, the M-P generalized inverse of $\boldsymbol{\Gamma}_1 \boldsymbol{\Gamma}_2$ exists, ensuring that control (28) is meaningful. Substituting control (28) into system (25) and left-multiplying both sides by $\boldsymbol{\Gamma}_1$ yields

$$\begin{aligned} \boldsymbol{\Gamma}_1 \ddot{\boldsymbol{v}} &= \boldsymbol{\Gamma}_1 \boldsymbol{a} + \boldsymbol{\Gamma}_1 \boldsymbol{\Gamma}_2 \underbrace{(\boldsymbol{\Gamma}_1 \boldsymbol{\Gamma}_2)^\dagger \hat{\boldsymbol{b}} + [\mathbf{I} - (\boldsymbol{\Gamma}_1 \boldsymbol{\Gamma}_2)^\dagger (\boldsymbol{\Gamma}_1 \boldsymbol{\Gamma}_2)] \mathbf{S}}_{P_{gen}} \\ &= \boldsymbol{\Gamma}_1 \boldsymbol{a} + \underbrace{\boldsymbol{\Gamma}_1 \boldsymbol{\Gamma}_2 (\boldsymbol{\Gamma}_1 \boldsymbol{\Gamma}_2)^\dagger \hat{\boldsymbol{b}}}_{\hat{\boldsymbol{b}}} + \underbrace{[\boldsymbol{\Gamma}_1 \boldsymbol{\Gamma}_2 - \boldsymbol{\Gamma}_1 \boldsymbol{\Gamma}_2 (\boldsymbol{\Gamma}_1 \boldsymbol{\Gamma}_2)^\dagger (\boldsymbol{\Gamma}_1 \boldsymbol{\Gamma}_2)] \mathbf{S}}_{\mathbf{0}} \\ &= \boldsymbol{\Gamma}_1 \boldsymbol{a} + \underbrace{\hat{\boldsymbol{b}}}_{\hat{\boldsymbol{b}} - \boldsymbol{\Gamma}_1 \boldsymbol{a}} \\ &= \boldsymbol{b}, \end{aligned} \quad (\text{A.4})$$

(Necessity): Suppose there exist some $(\mathbf{z}, \dot{\mathbf{z}}) \in \mathbb{R}^2 \times \mathbb{R}^2$ such that $\text{rank}(\boldsymbol{\Gamma}_1 \boldsymbol{\Gamma}_2) = 0$. This implies that $\boldsymbol{\Gamma}_1 \boldsymbol{\Gamma}_2 = \mathbf{0}$. Left-multiplying both sides of system (25) by $\boldsymbol{\Gamma}_1$ yields

$$\boldsymbol{\Gamma}_1 \ddot{\boldsymbol{v}} = \boldsymbol{\Gamma}_1 \boldsymbol{a} + \underbrace{\boldsymbol{\Gamma}_1 \boldsymbol{\Gamma}_2}_{\mathbf{0}} p = \boldsymbol{\Gamma}_1 \boldsymbol{a}, \quad (\text{A.5})$$

which contradicts the constraint (26). Therefore, for any $(\mathbf{z}, \dot{\mathbf{z}}) \in \mathbb{R}^2 \times \mathbb{R}^2$, it is necessary that $\text{rank}(\boldsymbol{\Gamma}_1 \boldsymbol{\Gamma}_2) \geq 1$. \square

Proof of Theorem 2. Let

$$\mathbf{V} = \mathbf{e}^T \mathbf{P} \mathbf{e}. \quad (\text{A.6})$$

For $\mathbf{P} > 0$, this is a valid Lyapunov candidate function, and its derivative is as follows

$$\begin{aligned} \dot{\mathbf{V}} &= 2\mathbf{e}^T \mathbf{P} \dot{\mathbf{e}} \\ &= 2\mathbf{e}^T \mathbf{P} (\mathbf{A} \ddot{\mathbf{z}} - \mathbf{b}) \\ &= 2\mathbf{e}^T \mathbf{P} \{ \mathbf{A} \mathbf{m}^{-1} [f(p_1 + p_2) - \tilde{c} \dot{\mathbf{z}} - \tilde{k} \mathbf{z} - \tilde{F}] - \mathbf{b} \} \\ &= 2\mathbf{e}^T \mathbf{P} \underbrace{[\mathbf{A} \mathbf{m}^{-1} (f p_1 - \tilde{c} \dot{\mathbf{z}} - \tilde{k} \mathbf{z} - \tilde{F}) - \mathbf{b}]}_{=0(\text{Thm.1})} + 2\mathbf{e}^T \mathbf{P} \mathbf{A} \mathbf{m}^{-1} f p_2. \end{aligned} \quad (\text{A.7})$$

Recalling Assumption 3, we have

$$\begin{aligned} \dot{\mathbf{V}} &= 2\mathbf{e}^T \mathbf{P} \mathbf{A} \mathbf{m}^{-1} f p_2 \\ &= 2\mathbf{e}^T \mathbf{P} \mathbf{A} \mathbf{m}^{-1} f (-\kappa_2 f^T \mathbf{m}^{-1} \mathbf{A}^T \mathbf{P} \mathbf{e}) \\ &= -2\kappa_2 \mathbf{e}^T (\mathbf{P} \mathbf{A} \mathbf{m}^{-1} f f^T \mathbf{m}^{-1} \mathbf{A}^T \mathbf{P}) \mathbf{e} \\ &\leq -2\kappa_2 \underline{\lambda} \|\mathbf{e}\|^2. \end{aligned} \quad (\text{A.8})$$

This means $\dot{\mathbf{V}} < 0$ for all $\mathbf{e} \neq 0$. As a result, we prove the asymptotic stability. \square

Data availability

No data was used for the research described in the article.

References

- [1] Y. Cai, L. Zhang, J. Zhang, et al., Bending-torsional vibration response of modified Timoshenko thin-walled beams under moving harmonic loads, *Appl. Math. Model.* 137 (2025) 115724, <https://doi.org/10.1016/j.apm.2024.115724>.
- [2] S. Li, D. Wang, C. Zhou, Multi-level structural optimization of thin-walled sections in steel/aluminum vehicle body skeletons, *Appl. Math. Model.* 132 (2024) 187–210, <https://doi.org/10.1016/j.apm.2024.04.050>.

- [3] H. Liu, C. Wang, T. Li, et al., Fixturing technology and system for thin-walled parts machining: a review, *Front. Mech. Eng.* 17 (4) (2022) 55, <https://doi.org/10.1007/s11465-022-0711-5>.
- [4] R. Zhao, Y. Jiao, X. Qu, Scaling design strategy for experimental rotor systems subjected to restricted support stiffness, *Appl. Math. Model.* 109 (2022) 265–282, <https://doi.org/10.1016/j.apm.2022.04.005>.
- [5] F. Dong, Z. Liu, X. Zhao, et al., Cooperative position and orientation modeling for dual-robot mirror milling under multi-source constraints, *Int. J. Adv. Manuf. Technol.* 131 (1) (2024) 315–328, <https://doi.org/10.1007/s00170-023-12915-8>.
- [6] B. Ding, J. Kong, W. Wang, et al., Investigation on a semi-active vibration attenuation device with follow-up support technology for mirror milling of thin-walled workpieces, *Mech. Syst. Signal Process.* 224 (2025) 112053, <https://doi.org/10.1016/j.ymssp.2024.112053>.
- [7] S. Liu, J. Xiao, W. Zhao, et al., Dynamic characteristics and chatter prediction of thin-walled workpieces in dual-robot mirror milling based on surrogate model of support parameters, *Mech. Syst. Signal Process.* 224 (2025) 112187, <https://doi.org/10.1016/j.ymssp.2024.112187>.
- [8] J. Xiao, Q. Zhang, H. Liu, et al., Research on vibration suppression by a multi-point flexible following support head in thin-walled parts mirror milling, *Int. J. Adv. Manuf. Technol.* 106 (2020) 3335–3344, <https://doi.org/10.1007/s00170-019-04728-5>.
- [9] S. Ma, J. Xiao, H. Liu, et al., Modeling and analysis for time-varying dynamics of thin-walled workpieces in mirror milling considering material removal, *Sci. China, Technol. Sci.* 66 (7) (2023) 1883–1898, <https://doi.org/10.1007/s11431-022-2360-6>.
- [10] Y. Bao, R. Kang, Z. Dong, et al., Model for surface topography prediction in mirror-milling of aircraft skin parts, *Int. J. Adv. Manuf. Technol.* 95 (2018) 2259–2268, <https://doi.org/10.1007/s00170-017-1368-9>.
- [11] J. Fei, B. Lin, S. Yan, et al., Chatter mitigation using moving damper, *J. Sound Vib.* 410 (2017) 49–63, <https://doi.org/10.1016/j.jsv.2017.08.033>.
- [12] L. Cen, S.N. Melkote, Effect of robot dynamics on the machining forces in robotic milling, *Proc. Manuf.* 10 (2017) 486–496, <https://doi.org/10.1016/j.promfg.2017.07.034>.
- [13] C. Ye, J. Yang, H. Ding, High-accuracy prediction and compensation of industrial robot stiffness deformation, *Int. J. Mech. Sci.* 233 (2022) 107638, <https://doi.org/10.1016/j.ijmecsci.2022.107638>.
- [14] W.C. Young, R.G. Budynas, A.M. Sadegh, *Roark's Formulas for Stress and Strain*, vol. 7, McGraw-Hill, New York, 2002.
- [15] G. Birkhoff, *Hydrodynamics*, vol. 2234, Princeton University Press, 2015.
- [16] P.I. Corke, W. Jachimczyk, R. Pillat, *Robotics, Vision and Control: Fundamental Algorithms in MATLAB*, Springer, Berlin, Heidelberg, 2011.
- [17] Q. Bo, H. Liu, M. Lian, et al., The influence of supporting force on machining stability during mirror milling of thin-walled parts, *Int. J. Adv. Manuf. Technol.* 101 (2019) 2341–2353, <https://doi.org/10.1007/s00170-018-3113-4>.
- [18] Y. Bao, X. Zhu, R. Kang, et al., Optimization of support location in mirror-milling of aircraft skins, *Proc. Inst. Mech. Eng., B J. Eng. Manuf.* 232 (9) (2018) 1569–1576, <https://doi.org/10.1177/0954405416673110>.
- [19] J. Lan, B. Lin, T. Huang, et al., Path planning for support heads in mirror-milling machining system, *Int. J. Adv. Manuf. Technol.* 91 (2017) 617–628, <https://doi.org/10.1007/s00170-016-9725-7>.
- [20] M.A. Johnson, M.H. Moradi, *PID Control*, Springer, 2005.
- [21] Y. Shtessel, C. Edwards, L. Fridman, et al., *Sliding Mode Control and Observation*, vol. 10, Springer, 2014.
- [22] S. Sastry, *Nonlinear Systems: Analysis, Stability, and Control*, vol. 10, Springer Science & Business Media, 2013.
- [23] Y.H. Chen, X. Zhang, Adaptive robust approximate constraint-following control for mechanical systems, *J. Franklin Inst.* 347 (1) (2010) 69–86, <https://doi.org/10.1016/j.jfranklin.2009.10.012>.
- [24] J. Han, P. Wang, F. Dong, et al., Optimal design of adaptive robust control for a planar two-dof redundantly actuated parallel robot, *Nonlinear Dyn.* 105 (3) (2021) 2341–2362, <https://doi.org/10.1007/s11071-021-06739-y>.
- [25] K. Huang, K. Shao, S. Zhen, et al., A novel approach for trajectory tracking control of an under-actuated quad-rotor uav, *IEEE/CAA J. Autom. Sin.* (2016), <https://doi.org/10.1109/JAS.2016.7510238>.
- [26] Z. Yang, J. Huang, H. Yin, et al., Path tracking control for underactuated vehicles with matched-mismatched uncertainties: an uncertainty decomposition based constraint-following approach, *IEEE Trans. Intell. Transp. Syst.* 23 (8) (2021) 12894–12907, <https://doi.org/10.1109/TITS.2021.3118375>.
- [27] Q. Sun, G. Yang, X. Wang, et al., Optimizing constraint obedience for mechanical systems: robust control and non-cooperative game, *Mech. Syst. Signal Process.* 149 (2021) 107207, <https://doi.org/10.1016/j.ymssp.2020.107207>.
- [28] H. Yin, D. Yu, S. Yin, et al., Possibility-based robust design optimization for the structural-acoustic system with fuzzy parameters, *Mech. Syst. Signal Process.* 102 (2018) 329–345, <https://doi.org/10.1016/j.ymssp.2017.09.037>.
- [29] F. Wang, S. Zhen, K. Chen, et al., Predefined performance control for fuzzy robotic systems with measurement noise: adaptation, robustness, and fuzzy optimization, *J. Franklin Inst.* 361 (11) (2024) 106956, <https://doi.org/10.1016/j.jfranklin.2024.106956>.
- [30] X. Chen, H. Zhao, H. Sun, et al., A novel adaptive robust control approach for underactuated mobile robot, *J. Franklin Inst.* 356 (5) (2019) 2474–2490, <https://doi.org/10.1016/j.jfranklin.2019.01.002>.
- [31] D. Fu, J. Huang, W.-B. Shangguan, et al., Constraint-following servo control for an underactuated mobile robot under hard constraints, *Proc. Inst. Mech. Eng., Part I, J. Syst. Control Eng.* 236 (1) (2022) 26–38, <https://doi.org/10.1177/09596518211024863>.
- [32] K. Huang, M. Wang, S. Zhen, Udwadia-Kalaba equation based adaptive robust control for two-wheeled inverted pendulum system: underactuation and uncertainty, *Int. J. Control. Autom. Syst.* 19 (7) (2021) 2420–2430, <https://doi.org/10.1007/s12555-019-1032-2>.
- [33] X. Chen, J. Ma, H. Sun, et al., Fuzzy-based controller synthesis and optimization for underactuated mechanical systems with nonholonomic servo constraints, *IEEE Trans. Fuzzy Syst.* 30 (10) (2022) 4152–4164, <https://doi.org/10.1109/TFUZZ.2022.3143003>.
- [34] D.J. Inman, R.C. Singh, *Engineering Vibration*, vol. 3, Prentice Hall, Englewood Cliffs, NJ, 1994.
- [35] B.K. Donaldson, *Introduction to Structural Dynamics*, Cambridge University Press, 2006.
- [36] D.-H. Yu, G. Li, H.-N. Li, Implementation of Rayleigh damping for local nonlinear dynamic analysis based on a matrix perturbation approach, *J. Struct. Eng.* 147 (9) (2021) 04021130, [https://doi.org/10.1061/\(ASCE\)ST.1943-541X.0003105](https://doi.org/10.1061/(ASCE)ST.1943-541X.0003105).
- [37] S. Onitsuka, Y. Ushio, N. Ojima, et al., Modeling method of element Rayleigh damping for the seismic analysis of a 3d fem model with multiple damping properties, *J. Vib. Control* 24 (17) (2018) 4065–4077, <https://doi.org/10.1177/1077546317718969>.
- [38] J. Chen, X. Zhang, *Algebraic Theory of Generalized Inverses*, Springer, Singapore, 2024.
- [39] W. Qin, F. Liu, P. Ge, et al., Fuzzy set theory for optimal design in controlling underactuated dynamical systems with uncertainty, *J. Vib. Control* 28 (5–6) (2022) 493–506, <https://doi.org/10.1177/1077546321990172>.
- [40] Y.H. Chen, Constraint-following servo control design for mechanical systems, *J. Vib. Control* 15 (3) (2009) 369–389, <https://doi.org/10.1177/1077546307086895>.